Design and experimental characterisation of a linear reciprocating generator

J.Wang
W.Wang
G.W.Jewell
D.Howe

XP-002327414

Abstract: The paper describes the design and experimental characterisation of a small reciprocating linear permanent-magnet generator which has been developed for on-board generation of electrical power for telemetry vibration monitoring systems. A comprehensive design methodology, which embraces both the electromagnetic and mechanical design, is described. The electromagnetic design synthesis is based around analytical field solutions which allow the optimisation of the generator parameters, and is further verified by nonlinear electromagnetic finite-element analysis. Nonlinear structural finite-element analysis is employed to aid the design of flexural disc springs with the desired stiffness and stroke. The utility of the design methodology is illustrated by a design study and extensive experimental characterisation of a prototype device.

List of principal symbols

A = magnetic vector potential, Wb/m

B = magnetic flux density, T

B_{rem} = remanence, T

f = frequency, Hz

H = magnetic field strength, A/m

I = output current, A

J = winding current density, A/m²

K_E = EMF constant, V·s/m

K_T = force constant, N/A

K_s = spring constant, N/m

L = winding inductance, H

M = remanent magnetisation, A/m

m = mass of plunger, kg

P_o = output power, W

R_L = load resistance, Ω

R_m = plunger radius, m

R_s = stator radius, m

z = axial displacement, m

μ_0 = permeability of free space, H/m

μ_r = relative recoil permeability

τ_p = pole pitch length, m

ω = angular frequency, rad/s

ψ_{wp} = winding flux linkage, Wb

1 Introduction

There are an increasing number of applications which demand the remote provision of low levels of electrical power and for which on-board power generation is preferable to the use of batteries, which have a limited lifetime and contain toxic materials [1]. For example, in telemetry-based condition vibration monitoring systems, where there is potential to utilise the inherent vibrations to generate the required electrical power via a reciprocating linear generator. In principle, any of the linear reciprocating actuator topologies that have been developed for use in applications ranging from automotive [2] to healthcare [3] may also be used for power generation. However, tubular machines with permanent-magnet excitation have a number of distinctive features [4], such as a high power density and a high efficiency, which make them particularly attractive for reciprocating linear generators.

This paper describes the design and experimental characterisation of such a small reciprocating linear permanent-magnet generator, shown in Fig. 1. It is a single-phase tubular device, which is capable of producing 20mW at 5V, with a nominal resonant frequency of 50Hz and a stroke of ±0.8mm. The two axially-magnetised sintered NdFeB magnets and the mild-steel pole pieces give rise to an essentially radial magnetic field in the region occupied by the generator winding. The moving permanent-magnet plunger is supported at each end by beryllium copper disc springs, which provide a high degree of radial stiffness, and an axial stiffness that can be accurately controlled by appropriate design of the spiral grooves. This spring plunger assembly mechanism also eliminates mechanical wear, and therefore results in improved reliability [5]. When the generator is vibrated, as shown schematically in Fig. 2, electrical power is generated as the result of the relative movement between the plunger and the winding. For a given amplitude of vibration,

IEE Proc.-Electr. Power Appl., Vol. 145, No. 6, November 1998

509

the system output power reaches a maximum when the frequency of the vibration matches the mechanical resonant frequency of the system.
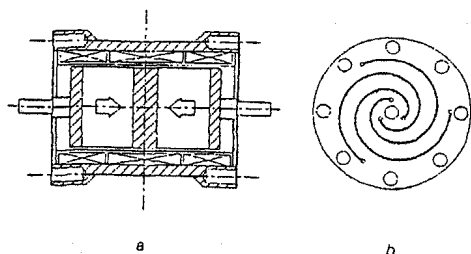

Fig. 1 *Reciprocating tubular linear permanent-magnet generator*
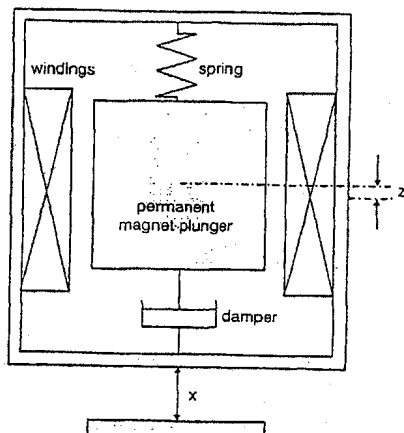*a* Linear generator
b Flexural spring

Fig. 2 *Schematic of reciprocating linear generator system*

To facilitate design optimisation and accurate dynamic modelling, a variety of techniques have been employed to predict the magnetic field distribution in tubular linear permanent-magnet machines [6], the most common approach being to employ a lumped equivalent circuit [7, 8]. While this allows the relationship between critical design parameters and machine performance to be established analytically, it suffers from problems associated with model inaccuracy, particularly when flux leakage is significant and the flux paths are complex. Therefore, numerical analysis of the field distribution and evaluation of performance [9, 10] is also employed. However, while techniques such as finite-element analysis provide an accurate means of determining the field distribution, with due account of saturation etc., they remain time consuming and do not provide as much insight as analytical solutions into the influence of the design parameters on the machine behaviour.

To overcome these problems, an analytical solution for the magnetic field distribution has been established in the cylindrical co-ordinate system [11]. It is an extension to the analysis which has been developed for tubular linear permanent magnet machines to account specifically for the relatively short stroke of reciprocating linear machines. The analytical solution allows the prediction of the thrust force and back-EMF in closed forms, which facilitates the characterisation of machines and provides a basis for design optimisation

and system dynamic modelling. The predicted results are verified by finite-element analyses and measurements on a prototype generator.

2 Field distribution due to permanent-magnet source

2.1 Magnetic field distribution
Fig. 3*a* shows the longitudinal section of the linear machine in which the axial length of the iron sleeve is usually longer than that of the plunger. To establish an analytical solution for the magnetic field distribution the following assumptions are made:

(i) The axial length of the machine is infinite and comprises an infinitely long iron sleeve and a series of segmented plungers extending to infinity along the machine axis, as shown in Fig. 3*b*.

(ii) The armature is slotless, and the permeability of the iron sleeve and pole pieces is infinite.

(iii) The relative recoil permeability of the magnets μ_r is 1.0.
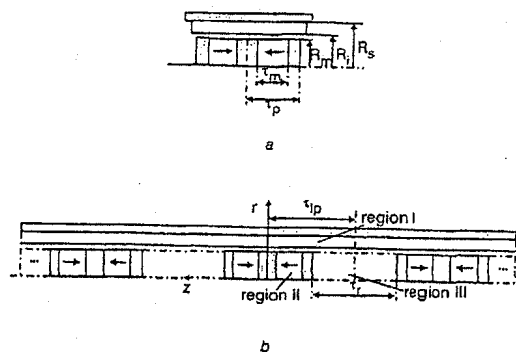

a

b

Fig. 3 *Analytical field models*
a Field model
b Extended field model

The magnetic field model of the actual linear generator may be represented by one of the repetitive elements in Fig. 3*b*, provided that the separation distance τ_r between two adjacent plungers is much greater than the pole pitch τ_p, i.e. $\tau_r \gg \tau_p$. Consequently, the magnetic field analysis is confined to three regions, viz. the airspace and winding regions *I* and *III* in which the permeability is μ_0, and the permanent-magnet region *II* in which the permeability is $\mu_0\mu_r$. To simplify the analysis, the regions *II* and *III* are combined by assuming that $\mu_{II} = \mu_{III} = \mu_0$, i.e. the airspaces between the plungers are filled by permanent-magnet material, but the magnets are only fully magnetised in region *II*, being unmagnetised in region *III*. Therefore

$$\mathbf{B} = \begin{cases} \mu_0 \mathbf{H} & \text{in region } I \\ \mu_0\mu_r\mathbf{H} + \mu_0\mathbf{M} & \text{in regions } II \text{ and } III \end{cases}$$

(1)

where **M** is the remanent magnetisation. For a permanent magnet having a linear demagnetisation characteristic, μ_r is constant and the magnetisation **M** is related to the remanence, B_{rem} by $\mathbf{M} = B_{rem}/\mu_0$. Further, for a rare-earth magnet $\mu_r \leq 1.10$. Hence, the assumption that $\mu_r = 1.0$ is justified. It is convenient to formulate the field distribution in terms of a magnetic vector potential A defined as $\mathbf{B} = \nabla \times \mathbf{A}$, and the cylindrical co-ordinate system shown in Fig. 4. The governing field

510

equations, in terms of the Coulomb gauge, $\nabla \cdot \mathbf{A} = 0$, are

$$\begin{cases} \nabla^2 \mathbf{A}_I = 0 & \text{in region } I \\ \nabla^2 \mathbf{A}_{II,III} = -\mu_0 \nabla \times \mathbf{M} & \text{in regions } II \text{ and } III \end{cases}$$
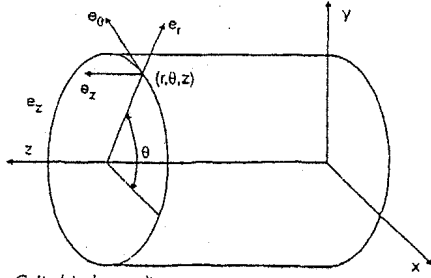
(2)

Fig.4 *Cylindrical co-ordinate system*

Since the field is axially-symmetric, $\mathbf{A}$ only has the component A_θ, which is independent of θ. This leads to

$$\begin{cases} \dfrac{\partial}{\partial z}\left(\dfrac{1}{r}\dfrac{\partial}{\partial z}(rA_{I\theta})\right) + \dfrac{\partial}{\partial r}\left(\dfrac{1}{r}\dfrac{\partial}{\partial r}(rA_{I\theta})\right) = 0 \\ \hspace{5cm} \text{in region } I \\ \dfrac{\partial}{\partial z}\left(\dfrac{1}{r}\dfrac{\partial}{\partial z}(rA_{II,III\theta})\right) + \dfrac{\partial}{\partial r}\left(\dfrac{1}{r}\dfrac{\partial}{\partial r}(rA_{II,III\theta})\right) \\ \hspace{3cm} = -\mu_0 \nabla \times \mathbf{M} \\ \hspace{3cm} \text{in regions } II \text{ and } III \end{cases}$$

(3)

In the cylindrical co-ordinate system, the flux density components are deduced from A_θ by

$$B_z = \frac{1}{r}\frac{\partial}{\partial r}(rA_\theta); \quad B_r = -\frac{\partial A_\theta}{\partial z}$$

(4)

The magnetisation $\mathbf{M}$ of the linear machine is
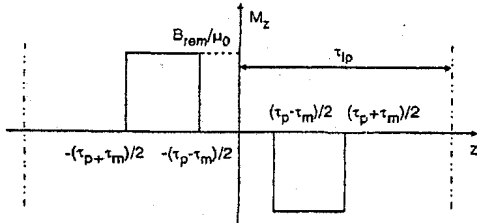
$$\mathbf{M} = M_z \mathbf{e}_z$$

(5)

Fig.5 *Magnetisation distribution*

where M_z as shown in Fig. 5 denotes the component of $\mathbf{M}$ in the z-direction, and may be expressed as the Fourier series

$$M_z = \sum_{n=1,2,\ldots} \frac{4B_{rem}}{\mu_0 \pi n} \sin\left(\frac{n\pi\tau_p}{2\tau_{lp}}\right)\sin\left(\frac{n\pi\tau_m}{2\tau_{lp}}\right)\sin m_n z$$

(6)

where τ_m is the axial length of the magnet, $\tau_{lp} = \tau_p + \tau_r/2$, and $m_n = n\pi/\tau_{lp}$. The boundary conditions to be satisfied by the solution to eqn. 3 are

$$B_{Iz}\big|_{r=R_r} = 0; \quad B_{II,IIIr}\big|_{r=0} = 0;$$

$$B_{IIr}\big|_{|z|=(\tau_p\pm\tau_m)/2} = 0; \quad B_{IIIr}\big|_{|z|=(\tau_{lp}-\tau_r/2)} = 0$$

$$B_{Iz}\bigg|_{\substack{r=R_m \\ |z|\leq(\tau_p-\tau_m)/2}} = 0; \quad B_{Iz}\bigg|_{\substack{r=R_m \\ (\tau_p+\tau_m)/2\leq|z|\leq\tau_p}} = 0$$

$$B_{Ir}\bigg|_{\substack{r=R_m \\ (\tau_p-\tau_m)/2\leq|z|\leq(\tau_p+\tau_m)/2}}$$
$$= B_{IIr}\bigg|_{\substack{r=R_m \\ (\tau_p-\tau_m)/2\leq|z|\leq(\tau_p+\tau_m)/2}}$$

$$H_{Iz}\bigg|_{\substack{r=R_m \\ (\tau_p-\tau_m)/2\leq|z|\leq(\tau_p+\tau_m)/2}}$$
$$= H_{IIz}\bigg|_{\substack{r=R_m \\ (\tau_p-\tau_m)/2\leq|z|\leq(\tau_p+\tau_m)/2}}$$

$$B_{Ir}\bigg|_{\substack{r=R_m \\ \tau_p\leq|z|\leq\tau_{lp}}} = B_{IIIr}\bigg|_{\substack{r=R_m \\ \tau_p\leq|z|\leq\tau_{lp}}}$$

$$H_{Iz}\bigg|_{\substack{r=R_m \\ \tau_p\leq|z|\leq\tau_{lp}}} = H_{IIIz}\bigg|_{\substack{r=R_m \\ \tau_p\leq|z|\leq\tau_{lp}}}$$

$$\int_0^{R_m} 2\pi r B_{IIz}\big|_{z=(\tau_p-\tau_m)/2} dr$$
$$= \int_0^{(\tau_p-\tau_m)/2} 2\pi R_m B_{Ir}\big|_{r=R_m} dz$$

(7)

Solving eqn. 3 subject to the boundary conditions of eqn. 7 yields

$$B_{Ir}(r,z)$$
$$= -\sum_{n=1,2,\ldots}^{\infty}[a_{In}BI_1(m_n r) + b_{In}BK_1(m_n r)]\cos(m_n z)$$

$$B_{Iz}(r,z)$$
$$= \sum_{n=1,2,\ldots}^{\infty}[a_{In}BI_0(m_n r) - b_{In}BK_0(m_n r)]\sin(m_n z)$$

(8a)

$$B_{IIr}(r,z)$$
$$= \sum_{i=1,2,\ldots}^{\infty}[a_{IIi}BI_1(q_{IIi}r)]\sin q_{IIi}(z - \tau_{II})$$

$$B_{IIz}(r,z)$$
$$= \sum_{i=1,2,\ldots}^{\infty}[a_{IIi}BI_0(q_{IIi}r)]\cos q_{IIi}(z - \tau_{II}) + B_0$$

(8b)

$$B_{IIIr}(r,z)$$
$$= \sum_{j=1,2,\ldots}^{\infty}[a_{IIIj}BI_1(q_{IIIj}r)]\sin q_{IIIj}(z - \tau_p)$$

$$B_{IIIz}(r,z)$$
$$= \sum_{j=1,2,\ldots}^{\infty}[a_{IIIj}BI_0(q_{IIIj}r)]\cos q_{IIIj}(z - \tau_p)$$

(8c)

where $BI_0(\cdot)$, $BI_1(\cdot)$ are modified Bessel functions of the first kind; $BK_0(\cdot)$, $BK_1(\cdot)$ are modified Bessel functions of the second kind, of order 0 and 1, respectively; q_{IIi}, q_{IIIj}, and τ_{II} are given by

$$q_{IIi} = \pi i/\tau_m; \quad \tau_{II} = (\tau_p - \tau_m)/2$$
$$q_{IIIj} = (2j - 1)\pi/\tau_r$$

(9)

and a_{In}, b_{In}, a_{IIi}, a_{IIIj}, and B_0 are defined in the Appendix

2.2 Comparison with finite-element calculations

The main design parameters of the reciprocating linear machine for which analytical field solutions have been

IEE Proc.-Electr. Power Appl., Vol. 145, No. 6, November 1998

511

obtained are given in Table 1. The magnets are sintered NdFeB with $B_{rem} = 1.2$T. The analytical field distributions have been validated by finite-element calculations of the radial and axial variations of the radial and axial flux density components in the airgap/winding regions.

Table 1: Parameters of reciprocating linear permanent-magnet generator

R_s (mm)	8.5	R_i (mm)	7.0
R_m (mm)	6.0	τ_{w1} (mm)	11.0
τ_p (mm)	11.0	τ_{w2} (mm)	7.5
τ_m (mm)	7.5	τ_r (mm)	44.0

The finite-element solutions were obtained by applying a periodic boundary condition at the axial boundaries $z = \pm \tau_{lp}$ and imposing the natural Neumann boundary condition at the surfaces of the stator sleeve and plunger iron pole pieces. Fig. 6 compares flux density components as functions of axial position z at a constant radius $r = 7.0$mm. It will be seen that the analytical solutions agree extremely well with the finite-element results.

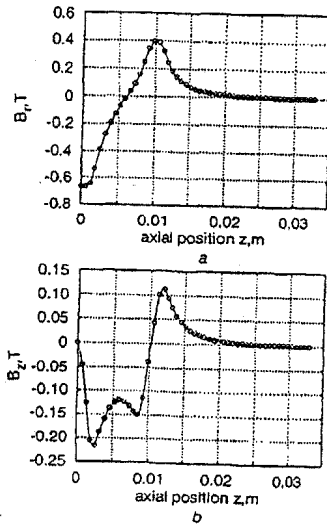**Fig. 6** *Flux density components as functions of axial position at $r = 0.007m$*
a Radial component
b Axial component
——— analytical
—▲— FEM

3 EMF and force prediction

3.1 Flux-linkage and EMF
Assuming that each coil of the armature winding comprises a number of circular turns, and occupies an area bounded by $r = R_i$, $r = R_s$, $z = z - \tau_w/2$, and $z_2 = z + \tau_w/2$, as shown in Fig. 7a, where τ_w is the coil axial width, the coil flux-linkage may be obtained from the following integration:

$$\psi_w = \int_{z-\tau_w/2}^{z+\tau_w/2} \int_{R_i}^{R_s} 2\pi r A_{10}(r,z) dr dz$$

$$= \sum_{n=1,2,...}^{\infty} \Phi_n \sin m_n z \qquad (10)$$

where

$$\Phi_n = \frac{4\pi}{m_n^2} \sin\left(m_n \frac{\tau_w}{2}\right)$$

$$\times \int_{R_i}^{R_s} r\left[a_{In} BI_1(m_n r) + b_{In} BK_1(m_n r)\right] dr$$

$$(11)$$

The total flux-linkage of the distributed armature winding, comprising coils 1, 2a and 2b, as shown in Fig. 7b, is therefore given by:

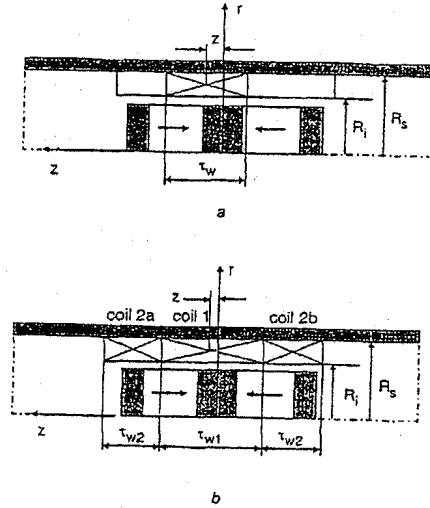$$\psi_{wp} = \psi_{w1} - (\psi_{w2a} + \psi_{w2b}) = \sum_{n=1,2,...}^{\infty} \Phi_{np} \sin m_n z$$

$$(12)$$

Fig. 7 *Distribution of armature winding*
a Coil distribution
b Winding distribution

where

$$\Phi_{np} = \frac{2\pi K_{dpn} N_{wp}}{m_n(R_s - R_i)}$$

$$\times \int_{R_i}^{R_s} r\left[a_{In} BI_1(m_n r) + b_{In} BK_1(m_n r)\right] dr$$

$$(13)$$

K_{dpn}, defined as the winding factor of the nth harmonic, is given by

$$K_{dpn} = $$
$$\frac{\sin(m_n \tau_{w1}/2) - 2\sin(m_n \tau_{w2}/2)\cos[m_n(\tau_{w1}+\tau_{w2})/2]}{m_n \frac{\tau_{w1}+2\tau_{w2}}{2}}$$

$$(14)$$

and N_{wp} is the number of series turns of the winding. Hence, the winding induced EMF is obtained as

$$e_{wp} = -\frac{d\psi_{wp}}{dt} = \left(-\sum_{n=1,2,...}^{\infty} K_{En} \cos m_n z\right) \frac{dz}{dt}$$

$$(15)$$

where K_{En} is analogously defined as the back-EMF constant of the nth harmonic, and is

512

$$K_{En} = \frac{2\pi K_{dpn} N_{wp}}{(R_s - R_i)}$$

$$\times \int_{R_i}^{R_s} r \left[a_{In} B I_1(m_n r) + b_{In} B K_1(m_n r) \right] dr$$

(16)

3.2 Thrust force

With reference to Fig. 7a, the thrust force exerted on the coil when it carries a current density J may be obtained from the following integration:

$$F_w = - \int_{z-\tau_w/2}^{z+\tau_w/2} \int_{R_i}^{R_s} 2\pi r J B_{Ir}(r, z) dr dz$$

which may be written as

$$F_w = \sum_{n=1,2,\dots}^{\infty} F_n \cos m_n z$$

(17)

where F_n is

$$F_n = \frac{4\pi J}{m_n} \sin \left(m_n \frac{\tau_w}{2} \right)$$

$$\times \int_{R_i}^{R_s} r \left[a_{In} B I_1(m_n r) + b_{In} B K_1(m_n r) \right] dr$$

(18)

The total force exerted on the distributed winding a carrying current J is therefore

$$F_{wp} = \left(\sum_{n=1,2,\dots}^{\infty} K_{Tn} \cos m_n z \right) I$$

(19)

where K_{Tn} is analogously defined as the force constant of the nth harmonic and is given by

$$K_{Tn} = \frac{2\pi K_{dpn} N_{wp}}{(R_s - R_i)}$$

$$\times \int_{R_i}^{R_s} r \left[a_{In} B I_1(m_n r) + b_{In} B K_1(m_n r) \right] dr$$

(20)

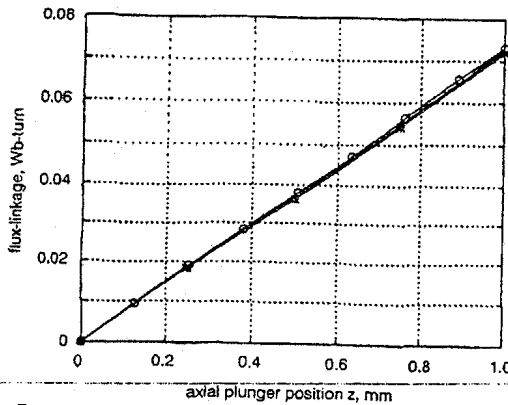which is identical to the EMF constant of the nth harmonic K_{En}.

Fig.8 *Flux-linkage as function of axial plunger displacement*
—— analytical
—O— measured
—*— FEM

3.3 Validation

Fig. 8 compares the measured winding flux-linkage of the single-phase reciprocating linear generator shown in Fig. 1a, whose design parameters were given earlier in Table 1, with the analytical and finite-element calculations. Both saturation and end-effects associated with the finite length of the stator sleeve are now accounted for in the finite-element calculation. However, as will be seen, the analytical prediction agrees well with both the finite-element and measured results, thus validating the developed analytical model for the linear machines, for which the computational times are significantly shorter than those required for corresponding finite-element analyses.

4 Design optimisation

4.1 Frequency response

As seen in Fig. 8, if the deflection z is small such that $\sin(m_n z) \simeq m_n z$, $(n = 1, 2, \dots, N)$, where N is the number of harmonic terms used for the calculation of the flux-linkage, ψ_{wp} is linear with respect to z. Thus, eqns. 15 and 19 may be simplified as

$$e_{wp} = -K_E \frac{dz}{dt}; \quad F_{wp} = K_T i$$

(21)

where K_E and K_T are defined as the EMF and force constants of the machine, respectively, and are

$$K_E = K_T = \sum_{n=1,2,\dots}^{N} K_{En}$$

(22)

Fig. 2 shows a simplified mechanical model of the linear power generation system. Assuming that the mass of the vibrating member, to which the generator housing is attached, is much greater than the mass of the plunger, so that the source of vibration is not affected by the plunger movement, the governing equations of the electromechanical system may be written as

$$\begin{cases} m \left(\frac{d^2 z}{dt^2} + \frac{d^2 x}{dt^2} \right) + K_s z + K_D \frac{dz}{dt} = K_T i \\ L \frac{di}{dt} + (R + R_L) i = -K_E \frac{dz}{dt} \end{cases}$$

(23)

where m is the plunger mass, K_s is the stiffness of the suspension spring, K_D is the damping factor, L and R are the inductance and resistance of the generator, respectively, and R_L is the load resistance. For a sinusoidal excitation vibration $x = \sqrt{2} X \sin \omega t$ the steady-state plunger deflection Z and output current I as functions of the vibration angular frequency ω are given, respectively, by

$$Z(\omega) = \frac{\omega^2 m X(\omega)}{(K_s - \omega^2 m) + j\omega \left[K_D + \frac{K_E^2}{j\omega L + R_T} \right]}$$

(24)

$$I(\omega) = -\frac{j K_E \omega}{j\omega L + R_T} Z(\omega)$$

(25)

where $R_T = R + R_L$. Fig. 9 shows Z, I and the output power $P_o = R_L I^2$ as functions of the vibration frequency f, assuming $X = 0.13$mm, $m = 0.020$kg, $K_E = 66.7$ V·s/m, $L = 0.15$H, $R = 1.5$kΩ, $R_L = 1.5$kΩ, $K_D = 0$, $K_s = 2000$N/m. The plunger deflection Z reaches its maximum amplitude approximately at the resonant frequency $\omega_c = \sqrt{(K_s/m)}$, which corresponds to the maximum output power for a given vibration amplitude.

4.2 Winding design

Since the generator employs a slotless armature the winding has a very low L/R ratio. Therefore eqn. 25

may be simplified as

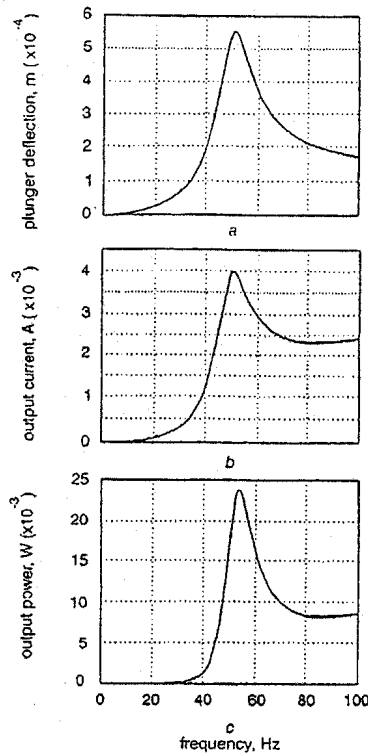$$I = \frac{K_E \omega}{R + R_L} Z \qquad (26)$$

Fig. 9 *Plunger deflection and output as functions of vibration frequency*
a Plunger deflection
b Output current
c Output power

From eqns. 16 and 22, the EMF constant K_E is proportional to the number of winding turns and may be expressed as

$$K_E = K_w N_{wp} \qquad (27)$$

where

$$K_w = \sum_{n=1,2,\ldots}^{N} \frac{2\pi K_{dpn}}{(R_s - R_i)}$$

$$\times \int_{R_i}^{R_s} r \left[a_{In} B I_1(m_n r) + b_{In} B K_1(m_n r) \right] dr \qquad (28)$$

The winding resistance R is also related to N_{wp} as follows:

$$R = K_r N_{wp}^2 \qquad (29)$$

where

$$K_r = \frac{\pi (R_s + R_i)\rho_{cu}}{P_f (R_s - R_i)(\tau_{w1} + 2\tau_{w2})} \qquad (30)$$

ρ_{cu} denotes the resistivity of copper, and P_f the winding packing factor. Thus, the output power to a resistive load R_L may be expressed as

$$P_o = I^2 R_L = \left[\frac{K_w N_{wp} Z \omega}{K_r N_{wp}^2 + R_L} \right]^2 R_L \qquad (31)$$

It can be shown that the optimal number of turns is given by

$$N_{wp} = \sqrt{R_L / K_r} \qquad (32)$$

which yields the maximum power output

$$P_{omax} = \frac{K_w^2}{4 K_r} (Z \omega)^2 \qquad (33)$$

Several observations can be made from the foregoing, *viz*:

(i) The output power is proportional to ω^2, implying that the specific power capability of the generator improves significantly as the vibration frequency increases.

(ii) At the resonant frequency the plunger displacement Z attains its maximum value, which is proportional to the magnitude of the acceleration $\omega^2 X$ of the vibration source. At this frequency the generator is most effective in converting the kinematic vibration energy into electrical energy. From this perspective, it is desirable to design the suspension spring such that the generator resonates at the frequency at which the acceleration of the vibration source is a maximum.

(iii) The output power is independent of the load resistance while being dependent on K_w and K_r which are related to the electromagnetic design parameters of the generator.
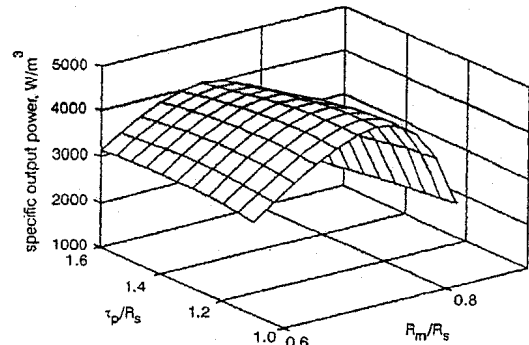

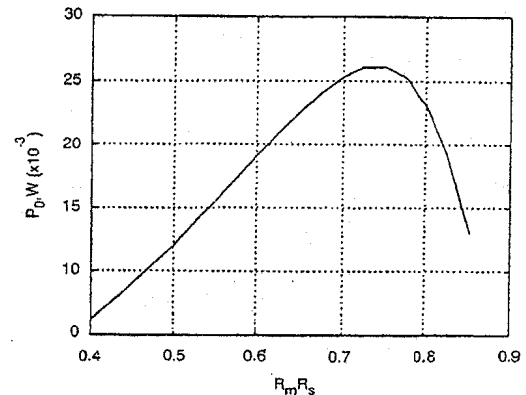**Fig. 10** *Specific power as function of R_m/R_s and τ_p/R_s*

Fig. 11 *Output power as function of R_m/R_s at $\tau_p = 0.011$ m*

4.3 Design optimisation

As pointed out earlier, the specific power capability of the generator can be maximised by selecting a set of optimal design parameters such that the ratio K_w^2/K_r reaches its peak for a given volumetric constraint. The

most influential design parameters for the machine topology shown in Fig. 1a are the ratios R_m/R_s and τ_p/R_s and therefore an optimal design can be achieved by scanning the two parameters. Fig. 10a shows the specific output power of the generator as a function of the ratios R_m/R_s and τ_p/R_s, assuming that $\tau_m/\tau_p = 0.7$, the airgap length $G = 1.0$ mm, $Z = 1.4$ mm, $R_s = 8.5$ mm, and $f = 20$ Hz, while Fig. 11 shows the generator output power as a function of R_m/R_s with $\tau_p = 11.0$ mm. The specific output power reaches its maximum at $R_m/R_s = 0.72$ and $\tau_p/R_s = 1.29$, and is more sensitive to the ratio of R_m/R_s than to τ_p/R_s.

5 Spring design

The suspension spring of the generator fulfils two basic functions: to replace linear bearings that are commonly used in linear machines so that the plunger is free from mechanical friction and wear, thereby resulting in improved reliability and efficiency; and to facilitate flexible axial plunger movement with a desired spring constant so that the generator resonates at a specified frequency. These require that the spring has a very high radial stiffness to withstand any unbalanced magnetic force due to mechanical and assembly tolerances, and a very low axial stiffness, particularly when resonating at a low frequency.

The suspension spring, shown in Fig. 1b, manufactured from beryllium copper sheet using photographic and etching processes, can meet these requirements. The central hole in the spring is a precise fit onto the plunger shaft. The radial and axial stiffnesses of the spring are affected by the thickness of the beryllium copper, and the number and length of the spiral grooves, one of whose trajectories is described by

$$\begin{aligned} x &= a\alpha\cos\alpha + x_0 \\ y &= a\alpha\sin\alpha + y_0 \end{aligned} \quad \alpha_0 \le \alpha \le \alpha_1 \quad (34)$$

For the three-groove configuration the trajectories of the other two grooves are obtained by rotating eqn. 34 by 120° and 240°, respectively. Hence, by varying the thickness of the sheet and the parameters a (x_0, y_0) and (α_0, α_1) in eqn. 34, it is possible to obtain the desired spring characteristic, which can be predicted by nonlinear structural finite-element analysis, using the package Ansys for example. Fig. 12 shows the deformation of a spring of 0.1 mm thickness, 8.5 mm radius, and having

0.32 mm wide grooves, under 1.0 N axial force, as predicted by Ansys. Fig. 13 compares the predicted and measured spring characteristics. As seen, the predicted and measured results are in reasonable agreement, the maximum error being 27% which may be attributable to the fact that the material properties used in the prediction may differ from those of the actual material. It is also observed that the spring exhibits some nonlinearity, which manifests itself as an increase in the spring stiffness as the deflection is increased.
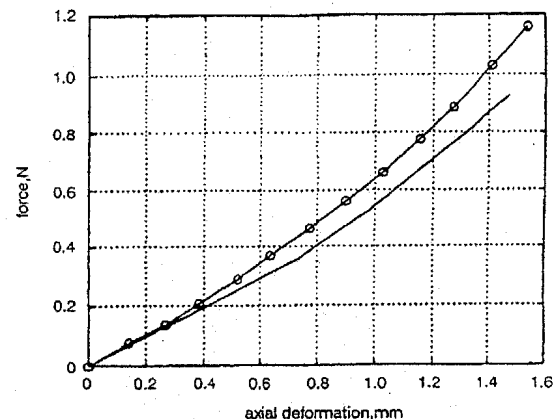
Fig. 13 *Comparison of measured and predicted spring characteristics*
——— predicted
—○— measured

Table 2: Specification and design parameters of reciprocating tubular linear permanent-magnet generator

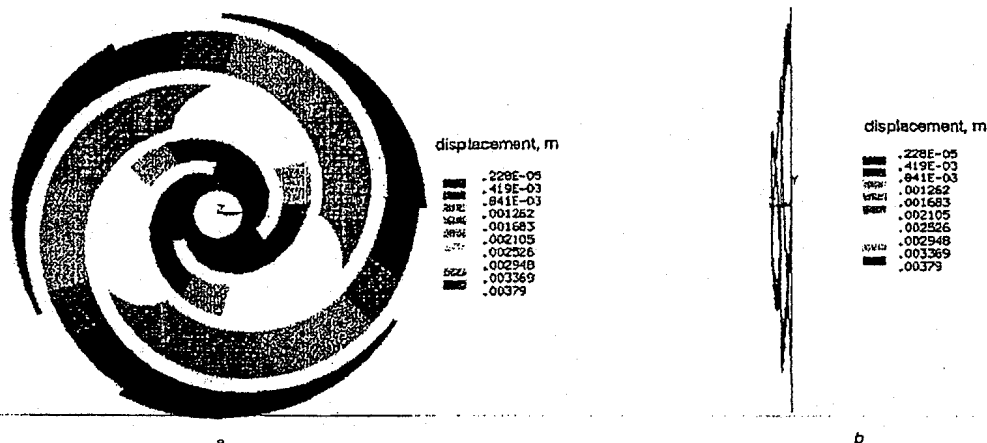| Specification		Design parameters	
Nominal output voltage, V	5.0	Armature radius R_s, mm	8.5
EMF constant, V·s/m	70.0	Magnet radius R_m, mm	6.0
Nominal deflection, mm	±0.8	Pole pitch τ_p, mm	11.0
Peak deflection, mm	2.0	Axial length of magnets τ_m, mm	7.5
Resonant frequency, Hz	50	Mass of plunder, g	18.9
Output power, mW	20	Airgap, mm	1.0

a

b

Fig. 12 *Predicted deformation of spring under 1 N axial load*
$a = 0.001$ m; $\alpha_0 = \pi/2$; $\alpha_1 = 17\pi/3$
a View from z-axis
b View from x-axis

IEE Proc.-Electr. Power Appl., Vol. 145, No. 6, November 1998

515

Table 3: Measured and predicted winding EMF constant, resistance and inductance

Winding parameters		EMF constant V•s/m		Resistance, 20°C (Ω)		Inductance, H	
No. of turns	Wire diam (mm)	Measured	Predicted	Measured	Predicted	Measured	Predicted
5900	0.063	72.3	71.8	1720	1750	0.171	0.163

6 Experimental results

A generator, whose specification and design parameters are given in Table 2, has been prototyped, Fig. 14. Its winding parameters, and measured and predicted EMF constant, resistance and inductance are given in Table 3. Measurements were carried out by mounting the generator to a voice-coil vibrator and applying a sinusoidal excitation. An accelerometer was attached to the vibrator to measure the input vibration. Since the input thrust force to the generator is proportional to the peak acceleration, most of the tests were conducted with constant peak acceleration so as to obtain comparative results.
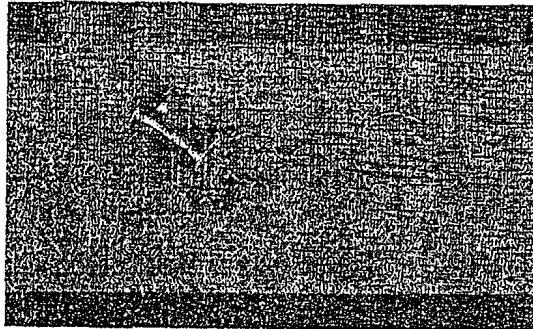

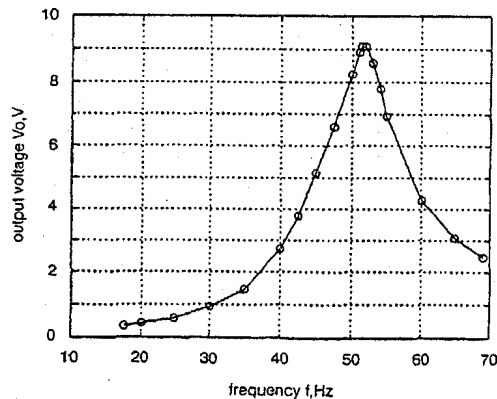**Fig. 14** *Prototype of reciprocating generator*

Fig. 15 *Open-circuit output voltage as function of vibration frequency under 0.382g peak input acceleration*

Fig. 15 shows the open-circuit output voltage as a function of the vibration frequency with 0.382g peak input acceleration. The open-circuit output voltage reaches its peak at a resonant frequency of 51 Hz. Fig. 16 shows the output voltage and power as functions of the vibration frequency with a 1.72 kΩ resistive load and 1.0g peak acceleration. Comparing with Fig. 15, although similar resonant behaviour is observed, the resonant frequency is now slightly lower at 46 Hz. This is attributed to the influence of the nonlinear spring characteristic shown in Fig. 13. On open-
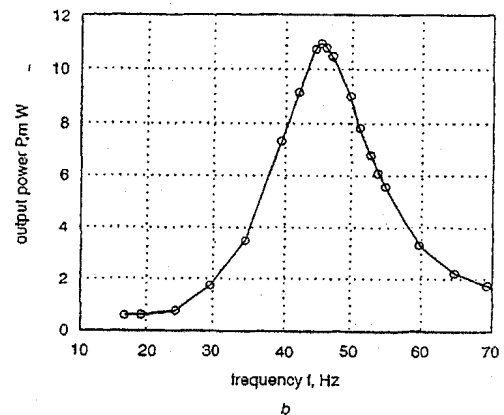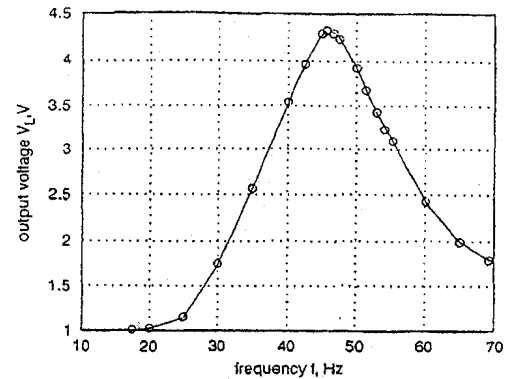

Fig. 16 *Output voltage and power as functions of vibration frequency with 1.72kΩ resistive load and 1.0g peak acceleration*
a Output voltage
b Output power

circuit, the effective damping is a minimum and a small input vibration may result in a larger deflection, a stiffer spring behaviour and therefore a higher resonant frequency. Fig. 17 shows a typical output voltage waveform and frequency spectrum when the generator is vibrated at 50 Hz frequency with the input acceleration waveform and frequency spectrum given in Fig. 18, again with a 1.72 kΩ resistive load. The output voltage is almost sinusoidal, the harmonic distortion being less than 4%, which again is largely due to the nonlinear spring effect. While this level of distortion is acceptable, there are other potential applications for the tubular generator topology for which the distortion might be one or two orders of magnitude too high. Velocity transducers, for example, for which the harmonic content could be reduced by appropriate signal conditioning. Fig. 19 shows the variation of the output voltage and power as functions of the input acceleration at the resonant frequency of 46 Hz, with the same resistive load. Theoretically, the output power is proportional to the square of the input acceleration, which is the case when the input acceleration is lower than

516

IEE Proc.-Electr. Power Appl., Vol 145, No. 6, November 1998

1.0g. However, as the magnitude of the input acceleration is increased, the nonlinear stiffness of the spring restricts the attainable deformation. As a consequence, the subsequent increase in output power become progressively lower than proportional to the square of acceleration.

7   Conclusions

A small reciprocating tubular linear permanent-magnet generator for use in applications such as on-board generation of electrical power on vibration transducers has been described, systematically analysed and
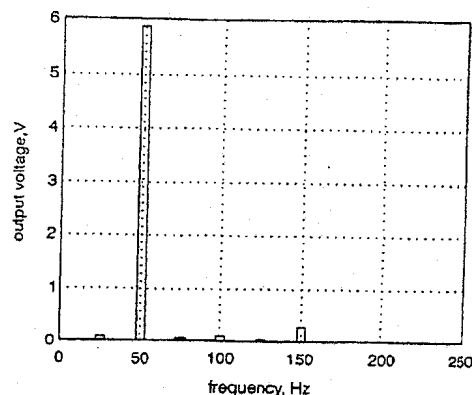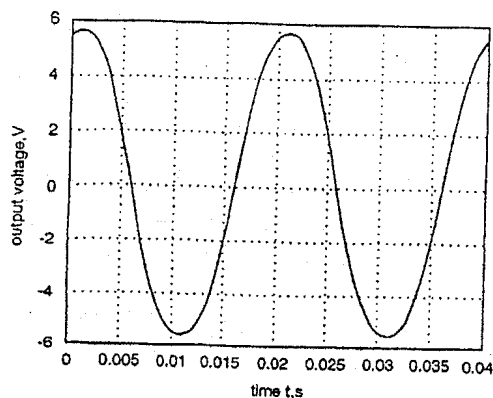

Fig. 17   *Typical output voltage waveform and frequency spectrum*
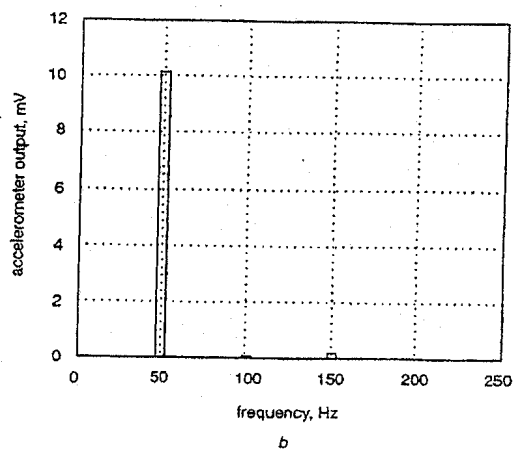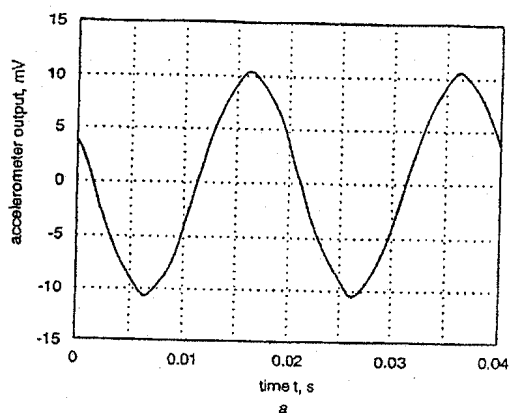a Output voltage
b Spectrum

Fig. 18   *Input acceleration waveform and frequency spectrum*
Sensitivity 10.6mV/g
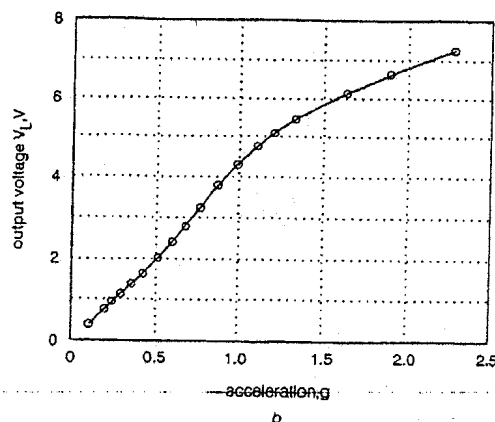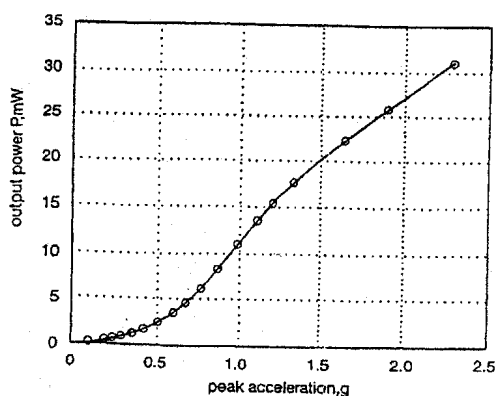a Input acceleration
b Spectrum

Fig. 19   *Output power and voltage as functions of input acceleration at resonant frequency, with 1.72kΩ resistive load*
a Output power
b Output voltage

IEE Proc.-Electr. Power Appl., Vol. 145, No. 6, November 1998

517

experimentally characterised. A complete electromechanical model of the power generation system has been established, and a design methodology to achieve maximum output power at a specified resonant frequency has been developed. The validity and effectiveness of the developed analysis and design technique have been confirmed by finite-element analysis and demonstrated on a prototype generator. The techniques are, by their general nature, applicable to reciprocating linear actuators of other topologies.

8 Acknowledgment

9 References

1 WILLIAMS, C.B., and YATES, R.B.: 'Analysis of a micro-electric generator for microsystems', *Sens. Actuators*, 1996, A52, pp. 8–11
2 LEQUESNE, B.: 'Permanent magnet linear motors for short strokes', *IEEE Trans. Ind. Appl.*, 1996, 32, (1), pp. 161–168
3 WATADA, M., YAMASHIMA, K., OISHI, Y., and EBIHARA, D.: 'Improvement on characteristics of linear oscillatory actuator for artificial hearts', *IEEE Trans. Magn.*, 1993, 29, (6), pp. 3361–3363
4 EASTHAM, J.F.: 'Novel synchronous machines: linear and disc', *IEE Proc. B*, 1990, 137, pp. 49–58
5 WHITE, M.A., COLENBRANDER, K., OLAN, R.W., and PENSWICK, L.B.: 'Generators that won't wear out', *Mech. Eng.*, 1996, 118, (2), pp. 92–96
6 BOLDEA, I., and NASAR, S.A.: 'Linear electric actuators and generators' (Cambridge University Press, 1997)
7 CLARK, R.E., SMITH, D.S., MELLOR, P.H., and HOWE, D.: 'Design optimisation of moving-magnet actuators for reciprocating electro-mechanical systems', *IEEE Trans. Magn.*, 1995, 31, (6), pp. 3746–3748
8 MIZUNO, T., and YAMADA, H.: 'Magnetic circuit analysis of a linear synchronous motor with permanent magnets', *IEEE Trans. Magn.*, 1992, 28, (5), pp. 3027–3029
9 AKMESE, R., and EASTHAM, J.F.: 'Dynamic performance of a brushless DC tubular drive system', *IEEE Trans. Magn.*, 1989, 25, (5), pp. 3269–3271
10 BASAK, A., and SHIRKOOHI, G.H.: 'Computation of magnetic field in D.C. brushless linear motors built with NdFeB magnets', *IEEE Trans. Magn.*, 1990, 26, (2), pp. 948–950
11 WANG, J., JEWELL, G.W., and HOWE, D.: 'A general framework for the analysis and design of tubular linear permanent magnet machines', submitted to *IEEE Trans. Magn.*

10 Appendix: Definition of a_{In}, b_{In}, a_{IIi}, a_{IIIj} and B_0

Let

$$c_{1n} = BI_0(m_n R_m); \quad c_{2n} = BK_0(m_n R_m)$$

$$c_{3n} = BI_1(m_n R_m); \quad c_{4n} = BK_1(m_n R_m)$$

$$c_{5n} = BI_0(m_n R_s); \quad c_{6n} = BK_0(m_n R_s)$$

$$c_{11i} = BI_1(q_{IIi} R_m); \quad c_{12j} = BI_1(q_{IIIj} R_m)$$

$$c_{21i} = BI_0(q_{IIi} R_m); \quad c_{22j} = BI_0(q_{IIIj} R_m)$$

$$c_{7n} = (2/m_n \tau_{lp})[\cos m_n \tau_{II} - \cos m_n(\tau_{II} + \tau_m)]$$

$$c_{8n} = (\sin m_n \tau_{II})/m_n$$

$$F_{inc} = \frac{2}{\tau_m} \int_{\tau_{II}}^{\tau_{II}+\tau_m} \cos m_n z \sin q_{IIi}(z - \tau_{II}) dz$$

$$F_{jnc} = \frac{4}{\tau_r} \int_{\tau_p}^{\tau_p + \tau_r/2} \cos m_n z \sin q_{IIIj}(z - \tau_p) dz$$

$$P_{nic} = \frac{2}{\tau_{lp}} \int_{\tau_{II}}^{\tau_{II}+\tau_m} \cos q_{IIi}(z - \tau_{II}) \sin m_n z dz$$

$$P_{njs} = \frac{2}{\tau_{lp}} \int_{\tau_p}^{\tau_p + \tau_r/2} \cos q_{IIIj}(z - \tau_p) \sin m_n z dz$$

$$d_{1n} = \left[\frac{c_{2n} c_{5n}}{c_{6n}} - c_{1n}\right]; \quad d_{2n} = \left[\frac{c_{4n} c_{5n}}{c_{6n}} + c_{3n}\right]$$

$$B_n = \frac{4 B_{rem}}{\pi n} \sin\left(\frac{n\pi \tau_p}{2\tau_{lp}}\right) \sin\left(\frac{n\pi \tau_m}{2\tau_{lp}}\right)$$

Then a_{In}, a_{IIi}, a_{IIIj} and B_0 are solutions of the following $(N_E + I_E + J_E + 1) \times (N_E + I_E + J_E + 1)$ linear equations:

$$d_{1n} a_{In} + \sum_{i=1}^{I_E}(P_{nis} c_{21i}) a_{IIi} + c_{7n} B_0$$

$$+ \sum_{j=1}^{J_E}(P_{njs} c_{22j}) a_{IIIj} = B_n$$

$$\sum_{n=1}^{N_E}(F_{inc} d_{2n}) a_{In} + c_{11i} a_{IIi} = 0$$

$$-\sum_{n=1}^{N_E}(d_{2n} c_{8n}) a_{In} + \sum_{i=1}^{I_E} \frac{c_{11i}}{q_{IIi}} a_{IIi} + \frac{R_m}{2} B_0 = 0$$

$$\sum_{n=1}^{N_E}(F_{jnc} d_{2n}) a_{In} + c_{12j} a_{IIIj} = 0$$

and

$$b_{In} = (c_{5n}/c_{6n}) a_{In}$$

where N_E, I_E and J_E are the numbers of the harmonic terms used for the calculation of the flux density in regions *I*, *II* and *III*, respectively.

518

IEE Proc.-Electr. Power Appl., Vol. 145, No. 6, November 1998